Experiments in Fluids (2024) 65:163
https://doi.org/10.1007/s00348-024-03908-8

RESEARCH ARTICLE

Quantitative near-field water–air spray measurements at elevated pressures by neutron radiography imaging

Aleksander Clark[1] · Walker Mccord[1] · Rajagopalan V. Ranganathan[1] · Yuxuan Zhang[2] · Jean-Christophe Bilheux[2] · Zhili Zhang[1]

Received: 21 June 2024 / Revised: 15 October 2024 / Accepted: 16 October 2024 / Published online: 1 November 2024

Abstract

Extensive experimental research on high-pressure spray has been conducted for decades to deepen our understanding and optimize its use in transportation, aviation, and propulsion applications; however, the near-field and in-nozzle flow characteristics are not fully understood. Dense near-field spray is among the most challenging diagnostic tasks since light is severely scattered and diffused by the liquid droplets and columns. In this work, the near-field spray and in-nozzle flow characteristics of an aeration nozzle at elevated pressures were characterized by neutron radiography imaging at the Oak Ridge National Laboratory High Flux Isotope Reactor. Neutron imaging benefits via strong penetration depths for some metals (i.e., aluminum, lead, and steel) and is sufficiently sensitive to detection of light elements, especially for hydrogen-based molecules, due to the large incoherent scattering cross section of neutrons. Both two-dimensional snapshots of the near-field spray and a three-dimensional tomographic scan of the nozzle geometry and in-nozzle water were obtained. This work provides new quantitative characterization of practical metal nozzle geometry for accurate boundary conditions, internal flow patterns inside the nozzle, and high-pressure spray flows. The findings may be used to improve performance and operating conditions of transportation vehicles and propulsion systems.

1 Introduction

The majority of the world's energy is derived from combustion, which has alone contributed to over 1 trillion tons of CO_2 emitted since the Industrial Revolution (Ritchie et al. 2020; Zhang et al. 2023). With a growing need for improving energy conversion systems for sustainability and emission reductions, many fundamental challenges stand as barriers to continued technical progress in liquid spray and its applications in transportation and propulsion systems, including lacking understanding of real-fluid effects, turbulence, and optical dense spray under elevated pressures. Among those, the fundamental understanding of flow physics in the spray under elevated pressures is of paramount importance.

✉ Zhili Zhang
zzhang24@utk.edu

[1] Mechanical, Aerospace and Biomedical Engineering, University of Tennessee-Knoxville, Knoxville, TN 37996, USA

[2] Neutron Scattering Division, Oak Ridge National Laboratory, Oak Ridge, TN 37890, USA

Spray diagnostics play a critical role in understanding the complexities involved in the process such as turbulence, secondary break-up, drop collisions, evaporation, and condensation (Bachalo et al. 2003; Danh et al. 2019; Durdina et al. 2014; Yue et al. 2001; Heindel 2018). Sprays are generally defined by two main regions: near-field and far-field. It is generally defined that the near-field region, or the spray formation region, typically represents the area beginning with the nozzle exit and moving in the direction of flow throughout the optically dense zone, and the far-field region typically begins when the spray has become sufficiently diluted (Fansler and Parrish 2015). A brief comparison of existing near-field spray diagnostics is given in Table 1. It should be noted that Table 1 is a partial list of existing spray diagnostic techniques with brief discussions of advantages and limitations, which is not an exhaustive list of all spray diagnostic techniques.

The optical diagnostics techniques of interest are shadowgraph, Schlieren imaging, laser-induced fluorescence (PLIF), particle image velocimetry (PIV), laser-induced phosphorescence (LIP), Rayleigh, Raman, and Mie scattering (Skeen et al. 2015; Thurow et al. 2013; Richard et al. 2001; Wu et al. 2000). Even though the techniques are good

Table 1 Limitations and advantages of various dense flow and spray diagnostics

Optical diagnostics (highly diffusive, optical dense)	• Shadowgraph and Schlieren, laser-induced fluorescence (PLIF), particle imaging velocimetry (PIV), laser-induced phosphorescence (LIP), Raman, Mie, Rayleigh scatterings, etc. (Thurow et al. 2013; Richard et al. 2001; Wu et al. 2000), interferometric imaging of phase Doppler particle analyzer (PDPA) (Vulgarakis Minov et al. 2016; Sijs et al. 2021), digital holography (Yao et al. 2021; Palero et al. 2007), structured laser illumination planar imaging (SLIPI) • Quantitative visualization of highly complex, unsteady flow fields (Lin et al. 2017; Bang and Lee 2013, 2015; Lee et al. 2013; Amirnordin et al. 2016) • Limited optical access, optical dense
Ballistic imaging	• Fs-laser-based imaging, ultrafast shutter to exclude multiple scattering • Penetrate dense spray regions (Linne 2013; Halls et al. 2017) • Photon scattering data loss increases with spray density
X-ray-based diagnostics	• X-ray phase-contrast imaging (PCI) (Linne 2013), X-ray radiography (Fansler and Parrish 2015), and X-ray fluorescence with tracers (Lin et al. 2014; Peltier et al. 2015), etc. • Hard to penetrate metals in general • X-ray can penetrate aluminum • Low sensitivity to hydrocarbons
Neutron imaging and radiography	• Metal nozzle geometry, in-nozzle flow measurement (Smith et al. 2018; Overberghe 2005) • Near-field dense spray measurement • Highly sensitive to hydrocarbon • Penetrate aluminum, steel and copper • Lower neutron flux compared to X-ray in general

at quantitative visualization of highly complex, unsteady flow fields, they are limited by their optical access and optical density. Another technique of interest is using ballistic imaging (Linne 2013; Halls et al. 2017), which were originally developed for medical applications. It uses Femtosecond-based laser for imaging and an ultrafast shutter to exclude multiple scattering. It is very helpful in penetrating dense spray regions but limited by the increase in photon scattering data loss with increasing density. Structured laser illumination planar imaging (SLIPI) uses modulated laser light to improve image clarity by reducing scattering effects, enabling precise visualization of spray distributions (Stiti et al. 2023; Berrocal et al. 2008).

X-ray-based diagnostics (Lin et al. 2014; Peltier et al. 2015; Kastengren and Powell 2014; Robert et al. 2010; Jang and Choi 2010; Matusik et al. 2018), such as phase-contrast imaging (PCI), radiography, and X-ray fluorescence, are common imaging techniques used in spray diagnostics. While these techniques are useful, the disadvantage is that it is hard to penetrate metals in general and has low sensitivity to hydrocarbons. Focused beam X-ray measurements have seen significant progress in recent years for extracting droplet Sauter mean diameter and surface area measurements. Combining X-ray measurements with techniques like phase-contrast imaging and ultrafast imaging has enabled capturing spray dynamics with great spatial and temporal resolutions (Vu et al. 2023).

Neutron imaging and radiography (Smith et al. 2018; Thimm et al. 2019; Takenaka et al. 2005; Lehmann et al. 2015; Duke et al. 2017) is a technique for spray diagnostic and has several applicable features such as: (1) ability to measure metal nozzle geometry, in-nozzle flow measurement, (2) near-field dense spray measurement, (3) highly sensitive to hydrocarbon, (4) penetrate aluminum, steel and copper and (5) limited neutron flux compared to X-ray. Though new, it is a well-understood method for characterizing fluid cavitation inside injection nozzles at elevated injection pressure. In our previous paper (Smith et al. 2018), the simultaneous neutron radiography of metal nozzle geometry and near-field spray was experimented at atmospheric conditions, which demonstrated proof-of-principle measurements for the spray diagnostics at elevated nozzle pressures. In this paper, neutron imaging was used to quantify practical metal nozzle geometry for accurate boundary conditions, internal flow patterns inside the nozzle, and high-pressure spray flows for a practical metal nozzle. The data could potentially be used to improve performance and operating conditions of transportation vehicles and propulsion systems.

2 Experimental setup and procedures

Figure 1 shows the schematics of the neutron imaging experimental setup used for neutron imaging experiments on liquid sprays under elevated pressures at the Multimodal Advanced Radiography Station (MARS) beamline at ORNL HFIR (Bardoel et al. 2011). The neutron source provides a polychromatic beam with energies ranging from thermal to epithermal neutrons. A series of collimators with different apertures were used to achieve the desired beam collimation and spatial resolution. The polychromatic neutron beam was used to illuminate the flow pattern of water spray through an

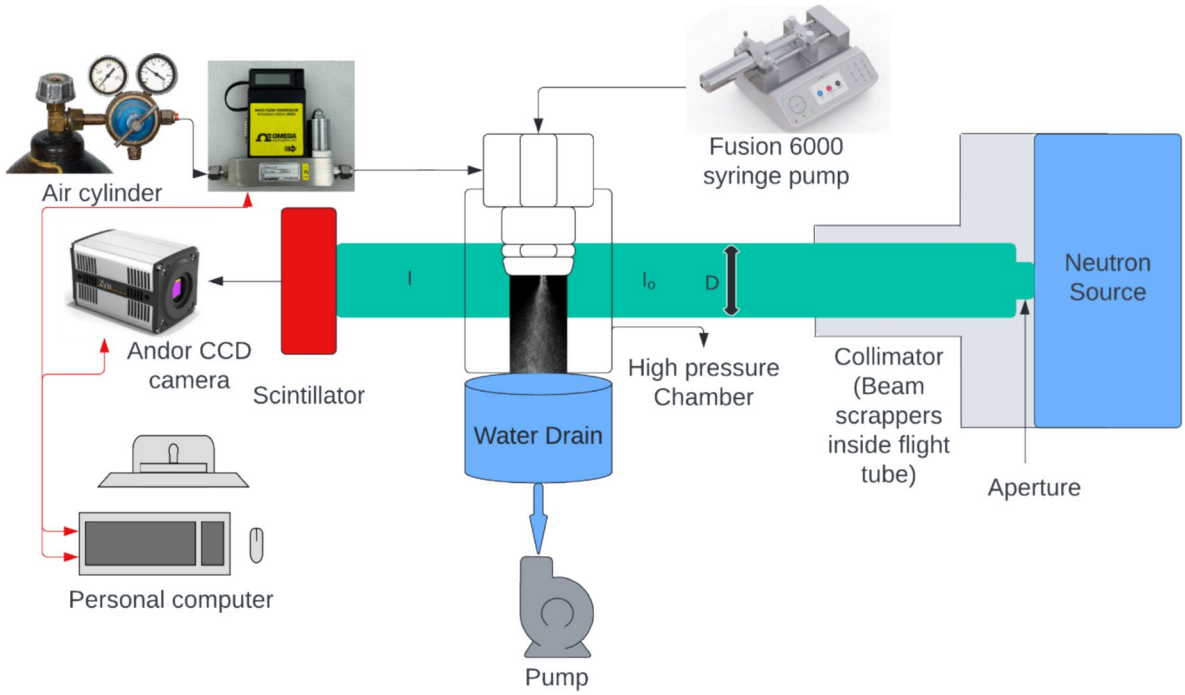

Fig. 1 Schematics of the experimental setup for neutron imaging of water spray at elevated pressures (not to scale)

air-assisted atomizing nozzle under elevated chamber pressures up to 5 bar_g (gage pressure). The nozzle was placed inside an aluminum chamber of 6-inch inner diameter, which was pressurized for tests between 0 and 5 bar_g. Though the chamber was designed for 8 bar_g, to ensure maximum safety of personnel the chamber was only pressurized to 5 bar_g. Also, water was used to simulate a fuel since it was the only approved liquid for the experiment. It employs 6LiF/ZnS scintillators with varying thicknesses (50–200 µm) to detect neutrons. Typical exposure times for the detecting camera ranged from 1 to 30 s, depending on the desired signal-to-noise ratio. The spatial resolution was measured to be approximately 0.05 mm.

As shown in Fig. 2, the aluminum chamber was designed and implemented for maximum neutron penetration, since aluminum is very transparent to neutrons compared to steel etc. (Schillinger 2000). Figure 2 provides detailed views of the experimental setup components. Figure 2a shows the aluminum pressure chamber used in the experiments, designed to enclose the nozzle with elevated pressures up to 8 bar_g. Figure 2b shows the chamber's cap, featuring chamber wall blowers to avoid mists on the chamber wall, an air feed line for air supply, a water feed line for injection, and the nozzle, detached from both air and water lines. This configuration allows precise control of the air and water flows. Additionally, a side viewing window is incorporated for high-speed imaging capabilities. A commercial Delavan oil-air atomizing nozzle is attached to the top plate and is lowered into the chamber, suspended for operation. A schematic of the nozzle used is shown in the supplemental material. Finally, Fig. 2c offers a zoomed view of the post-use and computed tomography (CT) exposure nozzle. The image reveals air feeds from the top and water feeds from the side. The nozzle overall length, not including the plugs, is 69 mm and measures 19 mm from plane to plane of 2 parallel faces of the hex body.

The nozzle and spray images were acquired using a charge-coupled device (CCD) coupled with a scintillator, converting transmitted neutrons into detectable photoemissions. Water was injected using a high-pressure syringe pump (Chemyx Fusion 6000-X) to deliver the necessary water pressure to overcome the chamber pressure. Some of the air used to pressurize the chamber was bled off to supply the air necessary for nozzle flow as well as supply air to blowers for the chamber walls to help mitigate water accumulation. The air run to the nozzle was controlled using a mass flow controller (Omega Engineering, FMA5528A) to adjust the injection velocity of the water stream as well as the liquid–air mixture.

Each test followed the same procedure adjusting the chamber pressure between 0 and 5 bar_g at 1 bar_g intervals, nozzle water flow at 0.05, 0.08, and 0.1 nominal liter per minute (nlpm), with constant air at 10 nlpm. Tests were performed at every variation of the chamber pressure and water flow rate. Air flow was adjusted and verified by first running

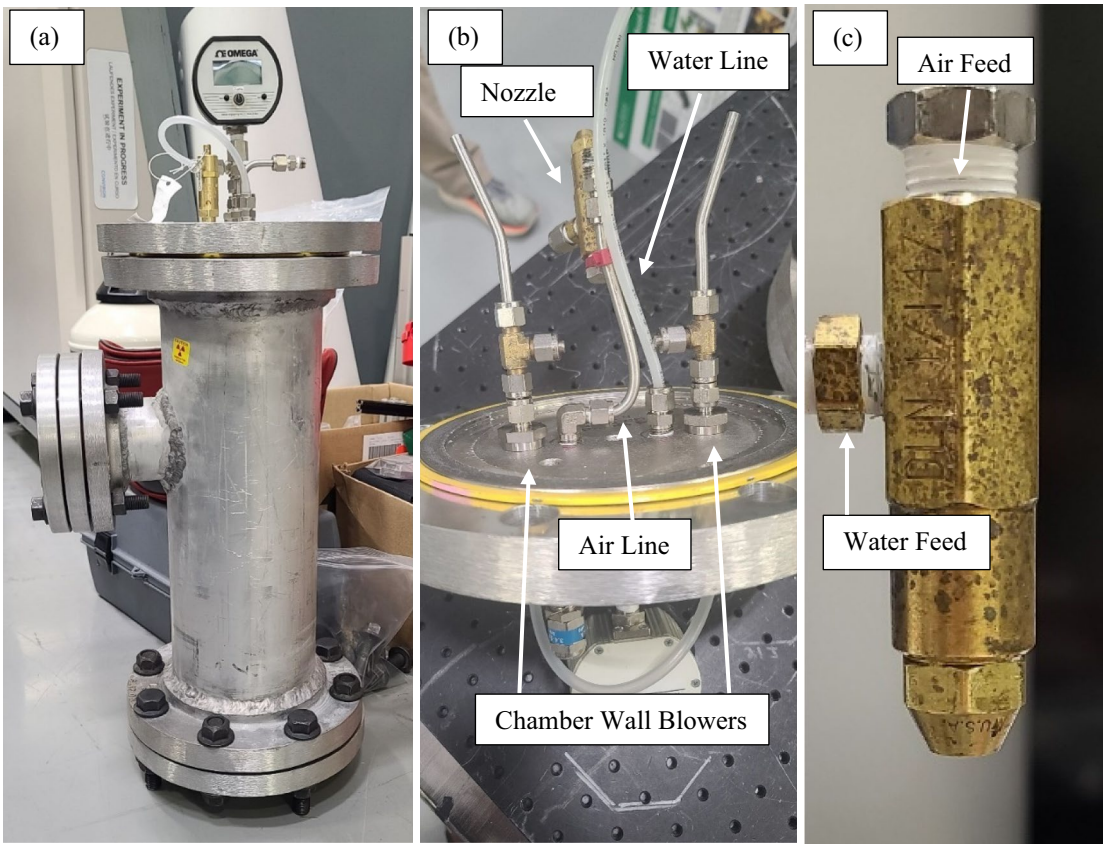

Fig. 2 **a** Aluminum pressure chamber (left); **b** Inside of cap featuring wall blowers, air feed, water feed and nozzle detached from feeds. **c** A zoomed picture of post-use and CT exposure nozzle with air feed plugged. Air feeds from the top; water feeds from the side

air through the nozzle. Since air flow was held constant, this only needed to be done once.

The chamber was placed in front of the beamline and run dry to calibrate imaging equipment and for alignment. Using the dedicated MARS data acquisition software, the aperture/pinhole size (D) and exposure time were adjusted to offer the best image. With the syringe filled with water and the injection lines primed to mitigate air pockets, the Fusion 6000-X syringe pump was programmed for a 30 s runtime for the appropriate injection volume with additional time and volume allotted for initialization and area lockdown. A drain pump for the excess water accumulated at the bottom of the chamber was turned on. This pulled the radiated water out while also keeping the chamber from over-pressurizing during the experiments. The main pressure control valve was opened and throttled to the desired chamber pressure, which was monitored by a digital pressure gage on the chamber. Once all parameters were set, the syringe pump was initialized, and the neutron beam area locked down. When verification of beam area lockdown was confirmed, the beam shutter was opened, and image capture began.

After each experiment, a radiation cool-down period was observed before approaching the chamber for operation safety purpose. Removal of the chamber cap was required to remove any excess water on the chamber walls before the next run could begin. The nozzle sample was examined to verify no leaks were occurring and the chamber was then resealed. The test procedure would then again be repeated as before for the varying parameters. All radiation guidelines and safety protocols were observed before, during and after each run.

For the 3D computed tomography (CT) image, representing a cross section view of the sample nozzle filled with water, the sample was removed from the chamber. The nozzle was filled with water and capped at the water and air ports, and wax was used to seal the nozzle exit end. Once confirmed that water was not leaking and filled to a reasonable level, it was stood up in an aluminum container on a rotating stage. Over the course of a few hours, the nozzle would rotate 360° to capture its 3D cross section. With each image being 30 s of exposure time and a step size of 0.31°, the total time for the CT scan was approximately 9 h and 41 min. All radiation guidelines and protocols were observed during this experiment.

3 Experimental results and discussions

3.1 Quantitative image analysis

The absorption and scattering of the neutron by material in a sample are measured as attenuation. By using the Beer–Lambert law, the neutron transmission is calculated as Raventos et al. (2017)

$$\frac{I(x_i)}{I_0(x_i)} = \int \exp^{[-\sum_{i=1}^{n}(\mu_i(\lambda)x_i)]} d\lambda \tag{1}$$

where λ and x_i are the wavelengths and the path length through the attenuating material, respectively. $I(x_i)$ and $I_0(x_i)$ are the transmitted and incident neutron intensities, respectively. The attenuation coefficient $\mu(\lambda)$ is given by the equation,

$$\mu(\lambda) = \sigma_{tot}(\lambda)\frac{\rho N_A}{M} \tag{2}$$

where $\sigma_{tot}(\lambda)$ is the total neutron attenuation cross section of the material, ρ is the density of the material in kg/m^3, N_A is Avogadro's number, and M is the molar mass.

The incident and transmitted neutron images of the attenuating material are normalized using the equation given below. This helps in correcting background noises, inhomogeneities of beam and detector, and fluctuation of neutron flux.

$$I_N = \frac{I_{(\text{raw image})} - I_{(\text{Dark Current})}}{I_{(\text{Open Beam})} - I_{(\text{Dark Current})}} \tag{3}$$

Equation 3 is used to obtain the normalized image. With the current neutron image settings, three different types of images are obtained: (1) no object in the field of view, (2) nozzle without injection, and (3) nozzle at different injection conditions. By using the ImageJ software package, the flat field normalization is obtained.

3.2 Comparison of sprays at different flow rates and pressures

The spray experiments were conducted at different pressure and water flow rates conditions. The exposure time for each run was 30 s. Three different nozzle flow rates were examined: 0.05 nlpm, 0.08 nlpm, and 0.1 nlpm of water, all in combination with 10 nlpm of air. These conditions were tested across chamber pressures ranging from 0 to 5 bar$_g$, as previously stated. While the manuscript presents data for the 0.08 nlpm condition, results for the other two flow rates (0.05 nlpm and 0.1 nlpm) are included in the supplementary materials. It should be noted that a dry run of nozzle without water was conducted, which is used as the background of the neutron imaging.

Figure 3 shows the normalized neutron images of spray under the water flow rate of 0.08 nlpm mixed with 10 nlpm of air as chamber pressures vary from 0 to 5 bar$_g$. The attenuation of the neutron by water is shown by the dark shade of gray. The volume with less attenuation is the lightest shade of gray. With neutron imaging, the presence of water inside the fuel injector is easily captured. Not only water but the liquid with H atom in the structure could be studied. With increasing pressures, a clear change in liquid penetration length is observed. At higher pressures, the spreading angle is narrow and steady. With decreasing flow rate, a clear trend in a decrease in liquid penetration length at all pressures is observed. The amount of water flow rate and pressure influences the availability of water inside the fuel injector. At low-pressure conditions, the higher flow rate of water leads to easy removal of water from the injector. This could be seen by less water availability near the bottom portion of the injector. With increasing pressure, the availability of water near the bottom surface becomes comparable.

Figure 4 shows the quantitative density of spray under different pressure and water flow rate conditions for the near-field region of the images taken. By using Eqs. 1–3, the density of the water–air mixture is quantified with a maximum resolution of 100 µm, per the limitations of the instrument configuration. A cone shape for the spray was assumed and utilized to calculate the water density. The 2D shape outline of the cone, which is a projection of the 3D spray into the camera, was obtained from the intensity changes in the neutron radiography image. The density at the nozzle exit is not 100% water because of the mixture of air and water, as per the design of the atomizing nozzle (Miller et al. 2021). Similar results were obtained by Distler et al. (2017) using a gasoline direct injection (GDI) nozzle and evaluating density using an X-ray technique. The maximum resolution was confirmed for the images captured using the dimensions of the nozzle.

Taking an average of the length (flow direction) of the results from Fig. 4, it can be more clearly seen the increase in water density approaches 250 kg/m^3 as the injection rate increases up to 0.1 nlpm, which is shown in Fig. 5. The red line features the cross section of the ROI where the maximum density value occurs, and the blue line the bottom where the supposed minimum will be as the water stream dissipates downstream of the exit. An average is also shown of the entire region of interest. Table 2 gives numerically the minimum and maximum values of the water density recovered from the region of interest.

The results from varying ambient pressures and liquid flow rates reveal the substantial impact of these parameters on spray geometry and density distribution. Chamber pressure profoundly influences spray behavior and

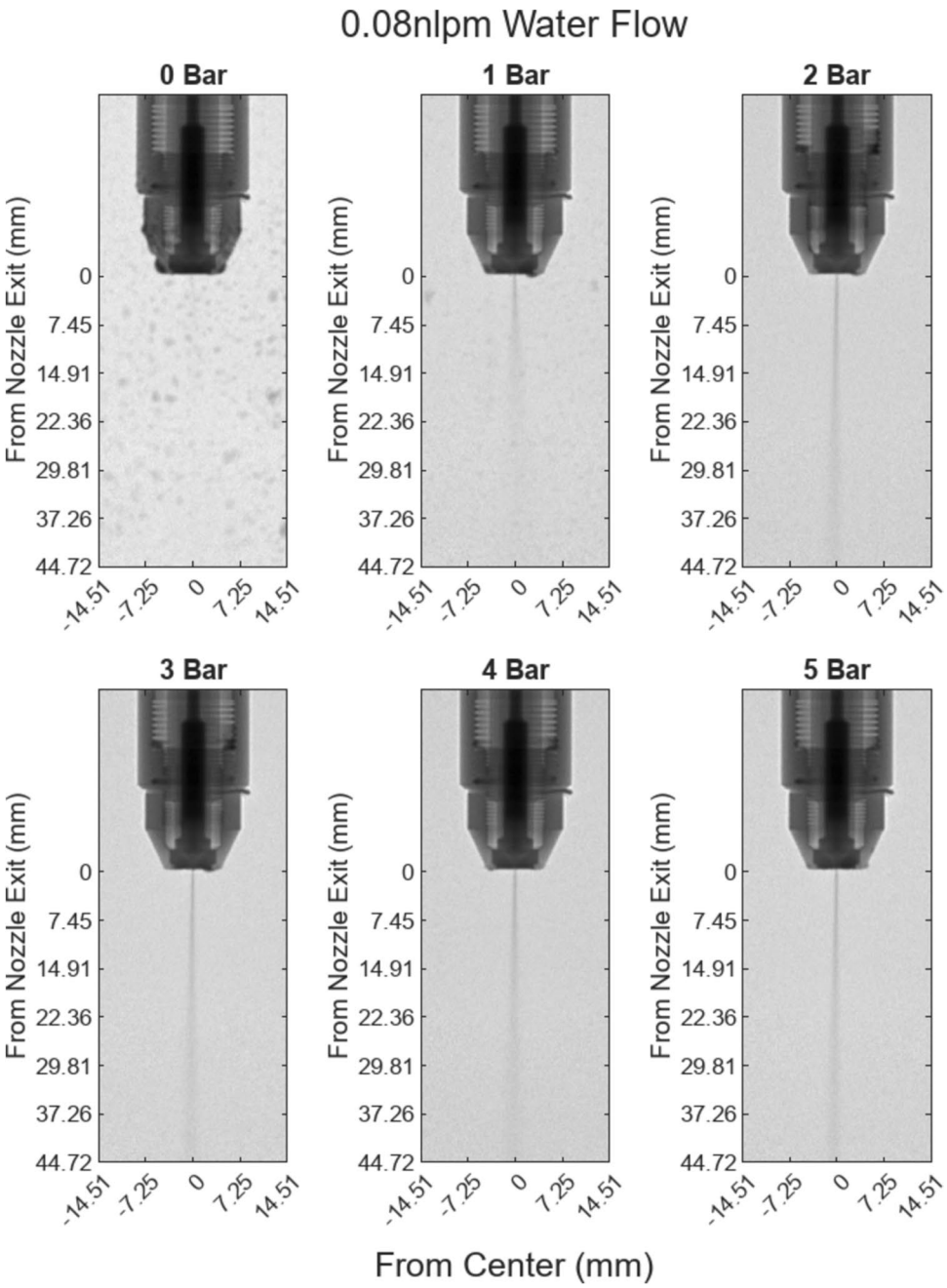

Fig. 3 Normalized neutron images captured by the camera. Water flow at 0.08 nlpm mixed with 10 nlpm of air between 0 and 5 bar_g chamber pressures. The measurements were conducted for a duration of 30 s to obtain time-averaged signal

characteristics. As pressure increases, changes in spray pattern and droplet density distribution become pronounced. At higher pressures, the spray cone angle narrows, producing a more focused and concentrated spray. In contrast, lower pressures widen the cone angle, leading to a more dispersed pattern. Density distribution within the spray also shifts with pressure variations. Higher pressures result in a denser cloud of droplets due to increased force driving finer atomization. Lower pressures, conversely, create a sparser distribution of droplets. Additionally increasing chamber pressure leads to deeper penetration due to higher velocity and finer droplets. Lower pressures reduce penetration depth. Velocity and momentum also follow this trend: higher pressures yield greater velocity and momentum, allowing the spray to travel farther before dispersing. Lower pressures limit travel distance.

The water flow rate also plays a key role in spray characteristics. Higher flow rates tend to result in a more substantial volume of liquid passing through the nozzle, leading to increased droplet formation and a denser spray cloud. This denser cloud can have implications for spray coverage and penetration depth. Lower water flow rates, on the other hand, may result in a sparser distribution of droplets, affecting the overall coverage and effectiveness of the

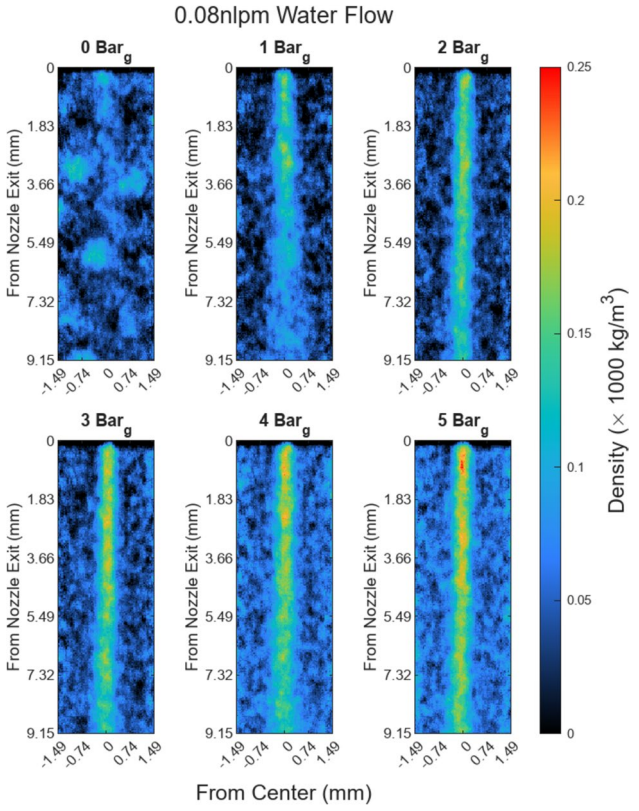

Fig. 4 Region of interest (ROI) at the atomizing nozzle exit. Water flow rate at 0.08 nlpm mixed with 10 nlpm of air. Water density shown varies up to 250 kg/m^3. The measurements were conducted for a duration of 30 s to obtain time-averaged signal

spray. Balancing water flow rates with chamber pressure is essential to achieve the desired spray characteristics, ensuring optimal coverage and penetration depth for specific applications.

Some dimensionless numbers can be used to characterize the fluid flow near-field to the nozzle exit. These numbers are the Reynolds number per unit length, the Weber number, and momentum flux of the fluid. The Reynolds number represents the ratio of the velocity to the kinetic viscosity of the fluid, which is described by,

$$\mathrm{Re}_{l_f} = \frac{U_f}{\nu_f} \tag{4}$$

where Re_{l_f} is the Reynolds number per unit length of the fluid, U_f is the fluid velocity, and ν_f is the fluid kinematic viscosity. For this experiment we assume that water is incompressible since the pressures we are applying do not have a significant effect on the viscosity; therefore, the kinematic viscosity of water is constant at $1002 \times 10^{-6} \frac{\mathrm{m}^2}{\mathrm{s}}$. The air, however, is affected by the pressure in the chamber, thus having an impact on its density. Equation (4) can be rewritten as,

$$\mathrm{Re}_{l_a} = \frac{U_a \rho_a}{\mu_a} \tag{5}$$

where in this case, Re_{l_a} is the Reynolds number per unit length of air, U_a is the velocity of air, ρ_a is the density of air, and μ_a is the dynamic viscosity of air at a constant $1.825 \times 10^{-5} \frac{\mathrm{kg}}{\mathrm{m \cdot s}}$, which is assumed independent of pressure. Density of the air varies with the pressure within the chamber as it flows out of the nozzle end. This is calculated using the ideal gas law,

$$\rho_a = \frac{P_{\mathrm{abs}}}{R \cdot T} \tag{6}$$

where P_{abs} is the absolute pressure in Pascals of the chamber, R is the gas constant for air at $287 \frac{\mathrm{J}}{\mathrm{kg \cdot K}}$, and T is the absolute temperature in the chamber which is assumed to be constant at 293K. Because the Reynolds number is dependent on velocity of the fluid, it was calculated using the ideal orifice exit of 2 mm diameter, by the manufacturer's standards. This value was used since only a theoretical velocity could be obtained from the 30 s averaged images. An error is applied to the value based on the maximum orifice diameter captured by the image's spatial resolution. Table 3 shows the ideal Reynolds number per unit length of the captured parameters with a spatial error of 8.5% across all values.

It can be noted from the table that there is very little variation in Reynolds number among the different water flow rates. This is a result of the dominating flow rate of air, which is the propelling fluid for the water. The ratio of momentum flux shows the ratio of the momentum of air to momentum of the liquid as expressed by,

$$M = \frac{\rho_a U_a}{\rho_f U_f} \tag{7}$$

where M is the momentum flux and ρ_f is the density of water at a constant $997 \frac{\mathrm{kg}}{\mathrm{m}^3}$. Table 4 shows the momentum flux for the varying water flow rates and chamber pressures.

As can be seen from Table 4, there is substantially higher water-to-air momentum present in the nozzle exit for the 0.05 nlpm water flow rate. What can also be noted is that the majority of momentum is dominated by the air, which again has a much greater flow rate over the water.

The Weber number is the ratio of the pressure force exerted by the liquid to surface tension of the liquid. This can be uniquely applied to atomizers by,

$$\mathrm{We} = \frac{\rho_a \left(U_f - U_a\right)^2 d}{\sigma} \tag{8}$$

where We is the Weber number, d is the orifice diameter in meters, and σ is the surface tension of water at $0.072 \frac{\mathrm{N}}{\mathrm{m}}$. Table 5 shows the Weber number for the varying conditions

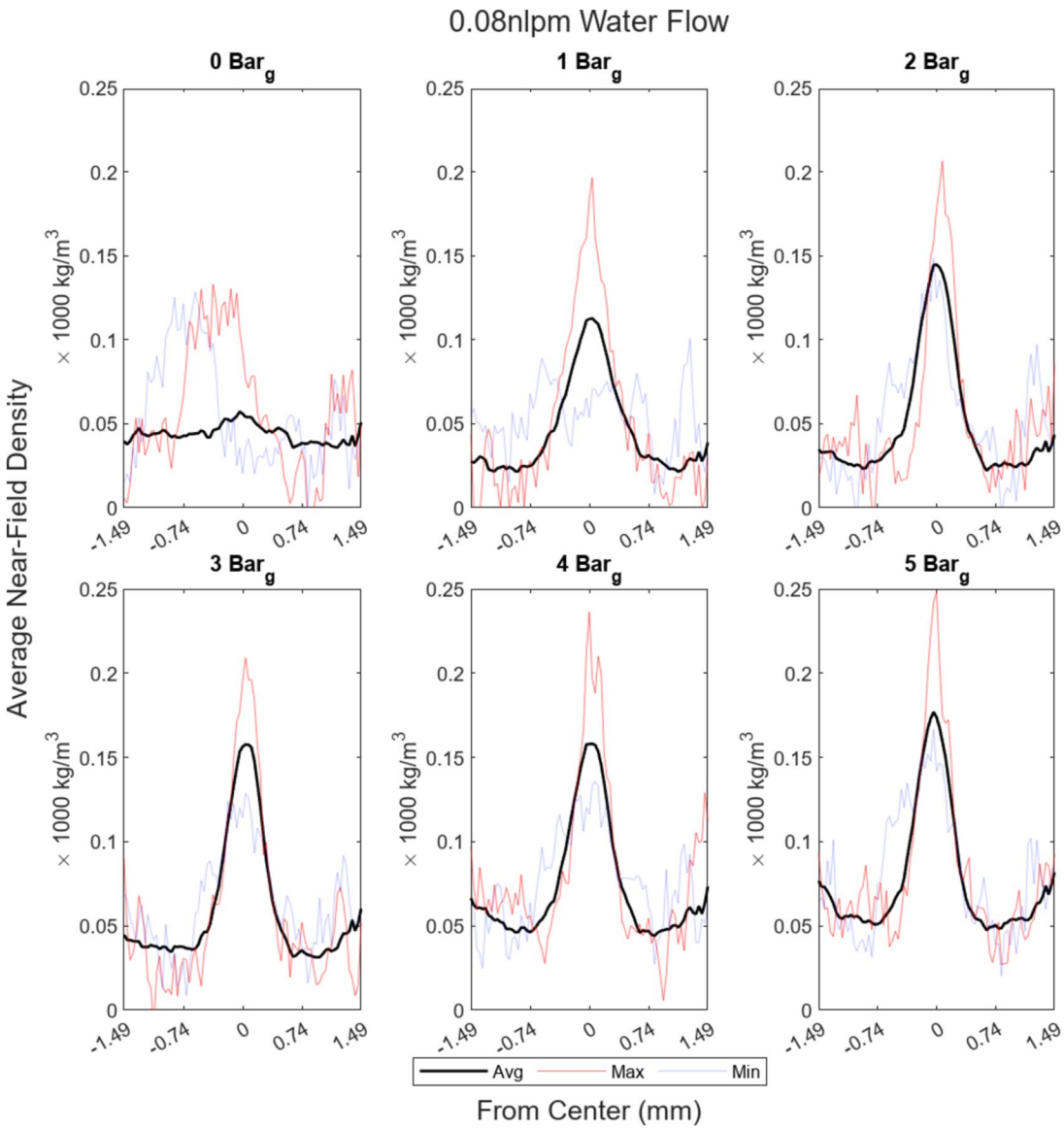

Fig. 5 The average near-field spray density over region of interest (ROI) along the flow length at the atomizing nozzle exit. Water flow rate at 0.08 nlpm mixed with 10 nlpm of air. The water density shown varies up to 200 kg/m^3 on average

Table 2 Minima–maxima and average water density at experimental conditions

Density [× 1000 kg/m^3]							
		0 bar$_g$	1 bar$_g$	2 bar$_g$	3 bar$_g$	4 bar$_g$	5 bar$_g$
0.05 nlpm	min	0	0	0.0116	0.0294	0.0572	0.0617
	max	0.0637	0.1118	0.1740	0.1855	0.1846	0.1970
0.08 nlpm	min	0	0.0354	0.0463	0.0724	0.0837	0.0705
	max	0.1303	0.1965	0.2064	0.2091	0.2366	0.2484
0.10 nlpm	min	0.1660	0	0.0031	0.0561	0.0752	0.0806
	max	0.1715	0.1591	0.2004	0.2063	0.2200	0.2330

Table 3 Reynolds number per unit length of air/water mixture. Values are 1×10^6/m

	0 bar_g	1 bar_g	2 bar_g	3 bar_g	4 bar_g	5 bar_g
0.05 nlpm	3.50297	6.95986	10.4168	13.8737	17.3306	20.7875
0.08 nlpm	3.50312	6.96002	10.4169	13.8738	17.3307	20.7876
0.10 nlpm	3.50323	6.96013	10.4170	13.8739	17.3308	20.7877

Table 4 Momentum flux of air/water mixture

	0 bar_g	1 bar_g	2 bar_g	3 bar_g	4 bar_g	5 bar_g
0.05 nlpm	48.3428	96.0534	143.764	191.474	239.185	286.896
0.08 nlpm	18.8839	37.5208	56.1578	74.7948	93.4317	112.068
0.10 nlpm	12.0857	24.01336	35.9410	47.8686	59.7963	71.7240

Table 5 Weber number of air/water mixture

	0 bar_g	1 bar_g	2 bar_g	3 bar_g	4 bar_g	5 bar_g
0.05 nlpm	93.2628	185.306	277.349	369.392	461.435	553.479
0.08 nlpm	92.7012	184.190	275.679	367.168	458.657	550.146
0.10 nlpm	92.3278	183.448	274.568	365.689	456.809	547.930

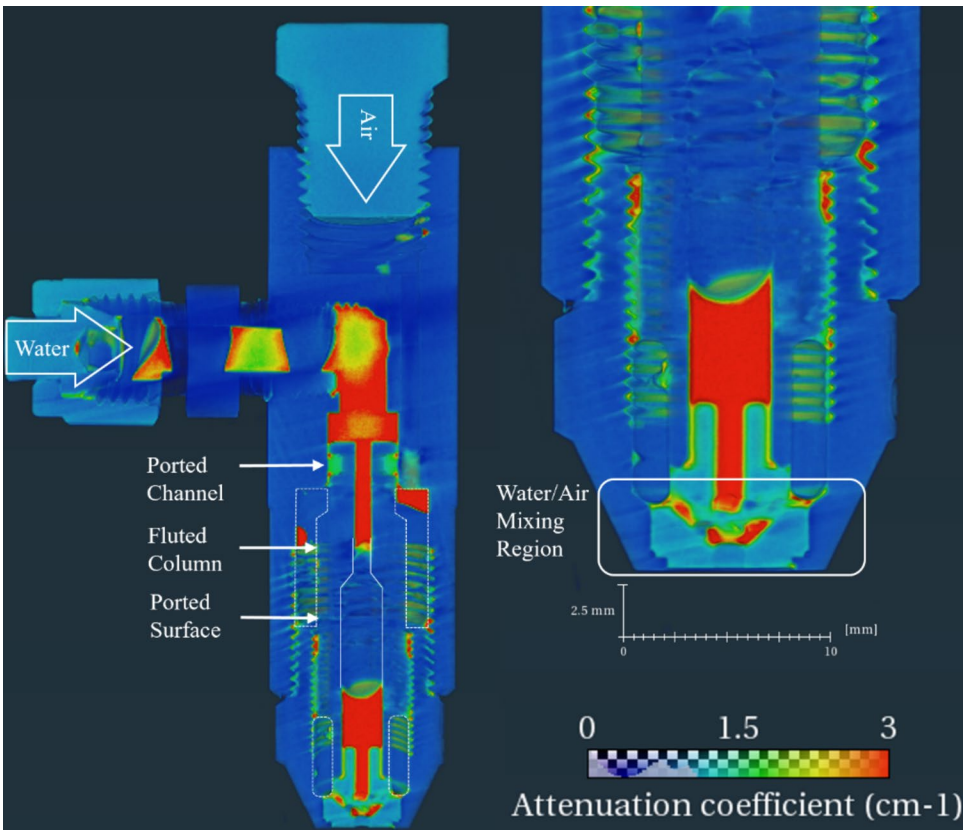

Fig. 6 Nozzle geometry shown where solid lines are water channels and dashed lines are air channels (**a**). Region of interest where the water and air mixture occurs (**b**). Higher attenuation coefficients signify water presence

applied to the nozzle. What can be noted here is the small impact the water flow rate has on the Weber number, but the large impact of the chamber pressure increases the liquid pressure to the surface tension.

3.3 Quantitative measurements of metal nozzle geometry and internal water distribution

The nozzle CT scan captured individual images of the nozzle

as it rotated from 0 to 360°. An image was captured every 0.31° of rotation. The images were then stitched together to form a three-dimensional tomography of the nozzle. Figure 6a shows the cross section of the nozzle, where various geometries are highlighted. Geometries noted are a ported channel where multiple orifices are present for air flow, a fluted column for air passage on the outside and water passage on the inside, and a ported surface that allows air through the removable nozzle end to enter the water/air mixing region.

Figure 6b zooms in on the mixing region of the nozzle. The color map shows the attenuation coefficient. The regions of interest such as water-filled nozzle show a higher attenuation coefficient, while the other regions made up of metals show lower values. A low attenuation region is present between two high-attenuation regions along the height of the nozzle. This is an air bubble trapped within the nozzle due to its geometry.

A detailed image of the water present in the nozzle via 3D tomography is shown in Fig. 7. This is only a physical representation of the water present within the nozzle, thus the nozzle itself was left mostly transparent. Water is present in the threading of the nozzle due to possible leaks, which could be attributed to manufacturing tolerances. The mixing region presents a "fan-like" shape for air flow to the end of the nozzle just before atomization would occur. This is only visible due to water entering these channels via the very tip. Had the nozzle been operating under flow conditions, these channels would not be easily visible. Air bubbles are also seen due to leakage that occurred during the hours-long CT scan. A short video of the 3D tomography as displayed by Fig. 7 can be found in Supplementary materials.

4 Conclusions

In conclusion, the data obtained from our experiments underscore the invaluable role of neutron imaging in studying the characteristics of injected sprays under elevated pressure environments. This significance is particularly highlighted by the fact that elevated pressure systems are often constructed with metal chambers for their strength under high pressures, making traditional X-ray imaging or some optical techniques impractical. Neutron imaging, with its ability to penetrate metal nozzles, offers a unique advantage for observing fluid characteristics within these structures and providing accurate measurements of metal nozzle geometry and internal water distribution.

Through the application of Beer–Lambert's law on neutron imaging, we were able to estimate the density of the

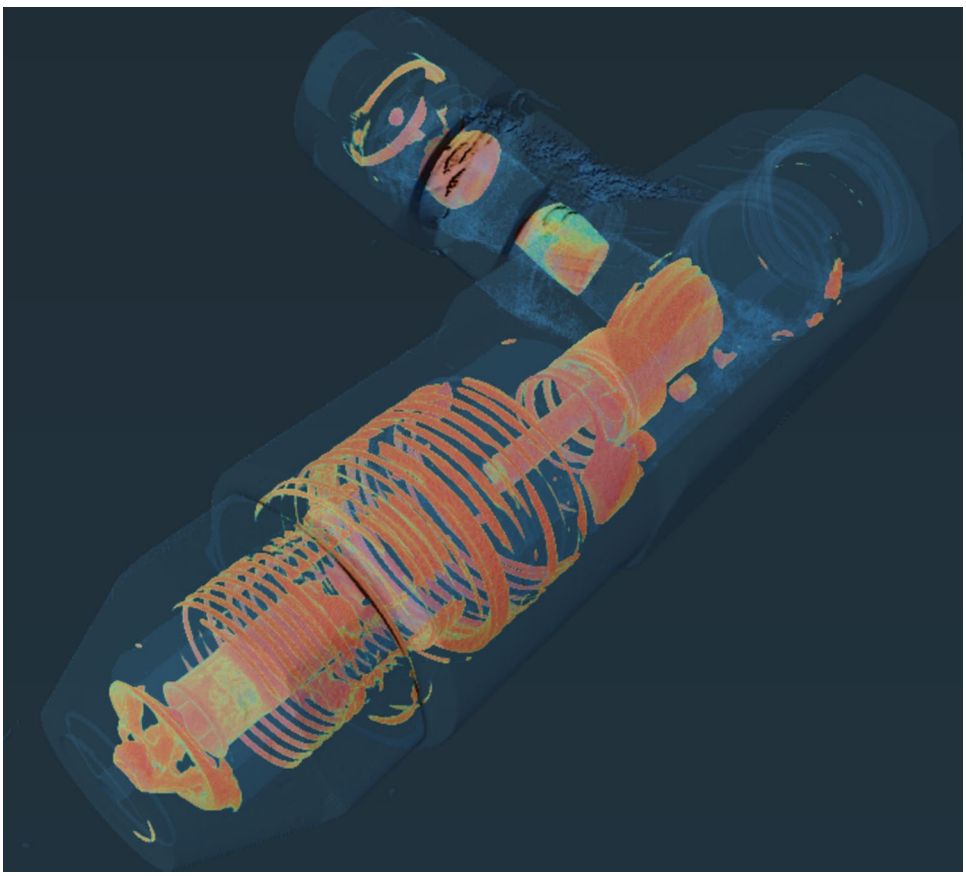

Fig. 7 3D tomography showing the water presence within the geometry of the nozzle with water in the highlighted voids

water-to-air mixture in the near field, providing crucial insights for predicting flow behavior and density in fuel injection systems operating at elevated pressures. Neutron radiography can effectively capture 3D internal flows within the nozzle, including the complex interactions between air and fluid, as well as the near-field dense flows. This makes it particularly useful for examining the detailed internal dynamics in such environments. These findings could not only contribute to the optimization of injection processes in high-pressure environments but also have broader implications for fields such as combustion engineering and fluid dynamics.

The limitations of neutron imaging arise from the relatively low neutron flux compared to X-rays, which necessitates longer exposure times to achieve a high signal-to-noise ratio. Neutron radiography is primarily effective for capturing average properties rather than resolving the turbulent structures inherent in high-speed sprays.

Supplementary Information The online version contains supplementary material available at https://doi.org/10.1007/s00348-024-03908-8.

Acknowledgements The work at University of Tennessee was supported by NSF and DOE. This research used resources at the High Flux Isotope Reactor, a DOE Office of Science User Facility operated by the Oak Ridge National Laboratory.

Author contribution A.C., W.M. and Y.Z. conducted the experiments, and A.C. and R.V.R. prepared figures. A.C., RVR and Z.Z. wrote the main manuscript text. All authors reviewed the manuscript.

Funding National Science Foundation.

Data availability No datasets were generated or analyzed during the current study.

Declarations

Conflict of interest The authors declare no competing interests.

References

Amirnordin SH, Khalid A, Sapit A, Salleh H, Razali A, Fawzi M (2016) Spray formation of biodiesel-water in air-assisted atomizer using Schlieren photography. In: IOP Conference Series: Materials Science and Engineering, vol 160. IOP Publishing. https://doi.org/10.1088/1757-899X/160/1/012032

Bachalo WD, Sankar SV (2003) Spray Diagnostics. In: Mercer CR (ed) Optical Metrology for Fluids, Combustion and Solids. Springer US, Boston, pp 133–173

Bang SH, Lee CS (2013) Comparison between background oriented Schlieren (BOS) technique and scattering method for the spray characteristics of evaporating oxygenated fuels. Optik 124(15):2147–2150

Bang SH, Lee CS (2015) Application of background oriented Schlieren (BOS) method for visualization of evaporating impinged spray. Optik 126(18):1606–1609

Bardoel AA, Counce D, Ekkebus AE, Horak C, Nagler S, Kszos L (2011) 2010 Neutron Review: ORNL Neutron Sciences Progress Report. Oak Ridge National Lab. (ORNL), Oak Ridge, TN (United States)

Berrocal E, Kristensson E, Richter M, Linne M, Aldén M (2008) Application of structured illumination for multiple scattering suppression in planar laser imaging of dense sprays. Opt Express 16(22):17870–17881

Danh V, Jiang L, Akinyemi OS (2019) Investigation of water spray characteristics in the near field of a novel swirl burst injector. Exp Thermal Fluid Sci 102:376–386

Distler R, Hamann C, Krämer M, Kull E, Wensing M, Li Z, Gao Y, Wang J (2017) High Speed X-Ray Imaging for Nozzle Exit Velocity and Density Distribution Measurements of GDI Nozzles

Duke DJ, Finney CE, Kastengren A, Matusik K, Sovis N, Santodonato L, Bilheux H, Schmidt D, Powell C, Toops T (2017) High-resolution x-ray and neutron computed tomography of an engine combustion network spray G gasoline injector. SAE Int J Fuels Lubr 10(2):328–343

Durdina L, Jedelsky J, Jicha M (2014) Investigation and comparison of spray characteristics of pressure-swirl atomizers for a small-sized aircraft turbine engine. Int J Heat Mass Transf 78:892–900

Fansler TD, Parrish SE (2015) Spray measurement technology: a review. Measur Sci Technol 26(1):012002 ((**34 pp**))

Halls BR, Radke CD, Reuter BJ, Kastengren AL, Gord JR, Meyer TR (2017) High-speed, two-dimensional synchrotron white-beam x-ray radiography of spray breakup and atomization. Opt Express 25(2):1605–1617

Heindel TJ (2018) X-ray imaging techniques to quantify spray characteristics in the near field. Atom Sprays 28(11):1029–1059

Jang SH, Choi SM (2010) Spray behavior of the rotary atomizer with in-line injection orifices. Atom Sprays 20(10):863–875

Kastengren A, Powell CF (2014) Synchrotron X-ray techniques for fluid dynamics. Exp Fluids 55(3):1686

Lee J, Kim N, Min K (2013) Measurement of spray characteristics using the background-oriented schlieren technique. Measur Sci Technol 24(2):025303 ((**9 pp**))

Lehmann E, Grünzweig C, Jollet S, Kaiser M, Hansen H, Dinkelacker F (2015) Visualisation of diesel injector with neutron imaging. J Phys: Conf Ser 656(1):012089

Lin K-C, Carter C, Smith S, Kastengren A (2014) Characterization of Aerated-Liquid Jets Using Simultaneous X-Ray Radiography and X-Ray Fluorescence Measurements. In: ILASS Americas 26th Annual Conference on Liquid Atomization and Spray Systems. Portland

Lin K-C, Lai M-C, Ombrello T, Carter C (2017) Structures and Temporal Evolution of Liquid Jets in Supersonic Crossflow. In: 55th AIAA Aerospace Sciences Meeting, AIAA SciTech Forum. AIAA: Grapevine, Texas

Linne M (2013) Imaging in the optically dense regions of a spray: a review of developing techniques. Prog Energy Combust Sci 39(5):403–440

Matusik KE, Duke DJ, Kastengren AL, Sovis N, Swantek AB, Powell CF (2018) High-resolution X-ray tomography of engine combustion network diesel injectors. Int J Engine Res 19(9):963–976

Miller M, Leick P, Köhler R, Kuhnhenn M, Samerski I, Lamanna G, Weigand B (2021) Characterisation of Internal Flow Conditions in GDI Injectors by Means of Spray-Hole-Individual Mass Flow Rate and Momentum Flux Measurements. International Conference on Liquid Atomization and Spray Systems (ICLASS)

Palero V, Arroyo MP, Soria J (2007) Digital holography for microdroplet diagnostics. Exp Fluids 43:185–195

Peltier S, Lin K-C, Carter C, Kastengren A (2015) Characterization of Flow Structures Inside an Aerated-Liquid Jet Using X-Ray Diagnostics. In: ILASS Americas 27th Annual Conference on Liquid Atomization and Spray Systems. Raleigh

Raventos M, Harti RP, Lehmann E, Grünzweig C (2017) A method for neutron scattering quantification and correction applied to neutron imaging. Phys Procedia 88:275–281

Richard BM, Walter RL, Joseph NF (2001) Laser Rayleigh scattering. Meas Sci Technol 12(5):R33

Ritchie H, Roser M, Rosado P (2020) CO_2 and greenhouse gas emissions. Our world in data

Robert É, Dozias SB, Cachoncinlle C (2010) Table-top flash X-ray diagnostics of dodecane sprays

Schillinger B (2000) Neutron tomography. In: Neutron Scattering in Novel Materials. World Scientific. pp 37–51

Sijs R, Kooij S, Holterman H, Van De Zande J, Bonn D (2021) Drop size measurement techniques for sprays: comparison of image analysis, phase Doppler particle analysis, and laser diffraction. AIP Adv 11(1):015315

Skeen SA, Manin J, Pickett LM (2015) Simultaneous formaldehyde PLIF and high-speed schlieren imaging for ignition visualization in high-pressure spray flames. Proc Combust Inst 35(3):3167–3174

Smith CD, Gragston MT, Zhang Z, Ombrello T, Carter CD, Tong X, Santodonato LJ, Bilheux HZ (2018) Simultaneous neutron radiography of metal nozzle geometry and near-field spray. J Propul Power 35(2):419–423

Stiti M, Garcia S, Lempereur C, Doublet P, Kristensson E, Berrocal E (2023) Droplet sizing in atomizing sprays using polarization ratio with structured laser illumination planar imaging. Opt Lett 48(15):4065–4068

Takenaka N, Kadowaki T, Kawabata Y, Lim I, Sim CM (2005) Visualization of cavitation phenomena in a Diesel engine fuel injection nozzle by neutron radiography. Nucl Instr Methods Phys Res Sect A Accel Spectrom Detect Assoc Equip 542:129–133

Thimm L, Trtik P, Hansen H, Jollet S, Dinkelacker F (2019) Experimental cavitation and spray measurement in real-size Diesel injection nozzles with high-resolution neutron imaging

Thurow B, Naibo J, Lempert W (2013) Review of ultra-high repetition rate laser diagnostics for fluid dynamic measurements. Meas Sci Technol 24(1):012002

Van Overberghe A (2005) High Flux Neutron Imaging for highly dynamic and time resolved non-destructive testing

Vu L, Machicoane N, Li D, Morgan TB, Heindel TJ, Aliseda A, Desjardins O (2023) A computational study of a two-fluid atomizing coaxial jet: Validation against experimental back-lit imaging and radiography and the influence of gas velocity and contact line model. Int J Multiph Flow 167:104520

Vulgarakis Minov S, Cointault F, Vangeyte J, Pieters JG, Nuyttens D (2016) Spray droplet characterization from a single nozzle by high speed image analysis using an in-focus droplet criterion. Sensors 16(2):218

Wu P, Lempert WL, Miles RB (2000) Megahertz pulse-burst laser and visualization of shock-wave/boundary-layer interaction. AIAA J 38(4):672–679

Yao L, Yu L, Lin X, Wu Y, Chen J, Zheng C, Wu X, Gao X (2021) High-speed digital off-axis holography to study atomization and evaporation of burning droplets. Combust Flame 230:111443

Yue Y, Powell CF, Poola R, Wang J-C, Schaller JK (2001) Quantitative measurements of diesel fuel spray characteristics in the near-nozzle region using X-ray absorption. Atom Sprays 11(4):471–490

Zhang S, Kaikun W, Yastrubskyi M, Huang C (2023) Carbon emissions from international trade and consumption: assessing the role of cumulative risk for EU and Chinese economic development. Energ Strat Rev 50:101219